COMMUNICATION

# Elusive Double Perovskite Iodides: Structural, Optical, and Magnetic Properties

Greggory T. Kent[a], Emily Morgan[a], Kaitlin R. Albanese[a][b], Anna Kallistova[a], Alexandra Brumberg[a], Linus Kautzsch[a], Guang Wu[b], Pratap Vishnoi[c], Ram Seshadri*[a] and Anthony K. Cheetham*[a][d]

[[a] Dr. G. T. Kent, E. Morgan, K. R. Albanese, Dr. A. Kallistova, Dr. A. Brumberg, L. Kautzsch, Prof. R. Seshadri, Prof. Sir A. K. Cheetham
Materials Department and Materials Research Laboratory
University of California
Santa Barbara, CA 93106 (USA)
E-mail: seshadri@mrl.ucsb.edu and akc30@cam.ac.uk
[b] Dr. G. Wu, K. R. Albanese
Department of Chemistry and Biochemistry
University of California
Santa Barbara, CA 93106 (USA)
[c] Prof. P. Vishnoi
New Chemistry Unit and International Centre for Materials Science
Jawaharlal Nehru Centre for Advanced Scientific Research (JNCASR)
Bangalore 560064 (India)
[d] Prof. Sir A. K. Cheetham
Department of Materials Science & Engineering
National University of Singapore
117576 Singapore (Singapore)

Supporting information for this article is given via a link at the end of the document.

**Abstract:** Halide double perovskites [$A_2M^IM^{III}X_6$] are an important class of materials that have garnered substantial interest as non-toxic alternatives to conventional lead iodide perovskites for optoelectronic applications. While numerous studies have examined chloride and bromide double perovskites, reports of iodide double perovskites are rare, and their definitive structural characterization has not been reported. Predictive models have aided us here in the synthesis and characterization of five iodide double perovskites of general formula $Cs_2NaLnI_6$ (*Ln* = Ce, Nd, Gd, Tb, Dy). The complete crystal structure, structural phase transitions, optical, photoluminescent, and magnetic properties of these compounds are reported.

Since their first reported use as photovoltaic (PV) materials in 2009,[1] hybrid lead iodide perovskites (e.g. $MAPbI_3$, MA = methylammonium) and their inorganic analogues have achieved remarkable performance benchmarks as active layers in PV devices.[2–6] However, due to the inherent toxicity and instability of the lead perovskites, there is great interest in finding lead-free perovskites with similar optical and electronic properties.[7] Aside from Pb(II), the only divalent *p*-block cations that can be incorporated into the perovskite framework are Ge(II) and Sn(II), which have stability issues of their own. A potential alternative to the halide perovskite structure ($AMX_3$) is the halide double perovskite, which adopts the general formula $A_2M^IM^{III}X_6$.[8,9] The double perovskite elpasolite framework permits substantial chemical diversity on its *M* sites, where alternating monovalent and trivalent *M* site metals allow extensive control over their electronic properties while offering non-toxic possibilities. This idea has stimulated the discovery of several new inorganic[8,10,11] and hybrid[9,12,13] chloride and bromide double perovskite compounds. Many of them use combinations of non-toxic Ag(I) and Sb(III) or Bi(III).[8,9,11] However, their use as alternatives to Pb(II) compounds in PV devices is limited by their wide and often indirect band gaps. Attempts to make $A_2M^IBiI_6$ and $A_2M^ISbI_6$ iodide double perovskite materials with narrower band gaps have been reported,[14–17] but their definitive existence has not been confirmed by structural characterization. One rationale for the lack of iodide double perovskite structures is the propensity for Bi(III) and Sb(III) compounds to form low dimensional 3:2:9 phases (i.e. $A_3Bi_2I_9$ and $A_3Sb_2I_9$) or face sharing chain structures that follow the 3D double perovskite formula.[18,19]

Recently, some of us addressed the paucity of iodide double perovskites by using the Goldschmidt tolerance factor (*TF*) in combination with the radius ratio of the trivalent $M^{III}$ cation to predict a large library of over 300 unknown inorganic and hybrid iodide double perovskites.[20] The results concluded that while most trivalent $M^{III}$ cations are too small to support octahedral coordination by iodide anions in a double perovskite structure, this should be feasible by using rare earth cations in the $M^{III}$ site. Inorganic chloride and bromide double perovskites containing rare-earths are relatively common,[21–25] and two hybrid double perovskites, $(MA)_2KGdCl_6$ and $(MA)_2KYCl_6$,[26] have been reported. In terms of iodide double perovskites, Meyer reported the synthesis of $Cs_2LiLnI_6$ (*Ln* = Sc, Lu, Tm, Ho) and $Cs_2NaLnI_6$ (*Ln* = Sc, Lu, Tm, Er) in 1980, but their complete structures were not provided.[27] $Cs_2NaLaI_6$ and $Cs_2NaLaI_6$:2% Ce have also been investigated as possible x-ray scintillators, but again their full structural characterization has not been reported.[28,29]

Here we report the solid-state synthesis of a series of lanthanide iodide double perovskites following the general formula $Cs_2NaLnI_6$ (*Ln* = Ce, Nd, Gd, Tb, Dy). Their structures, compositions, and structural transitions have been studied by single crystal X-ray diffraction, synchrotron X-ray powder diffraction, and differential scanning calorimetry. Optical absorption, photoluminescent, and magnetic properties are also detailed.

The compounds were synthesized *via* solid-state reaction of the appropriate $LaI_3$ with 2 equivalents of CsI and 1 equivalent of NaI at 675 ºC in an alumina crucible, under strictly air-free and

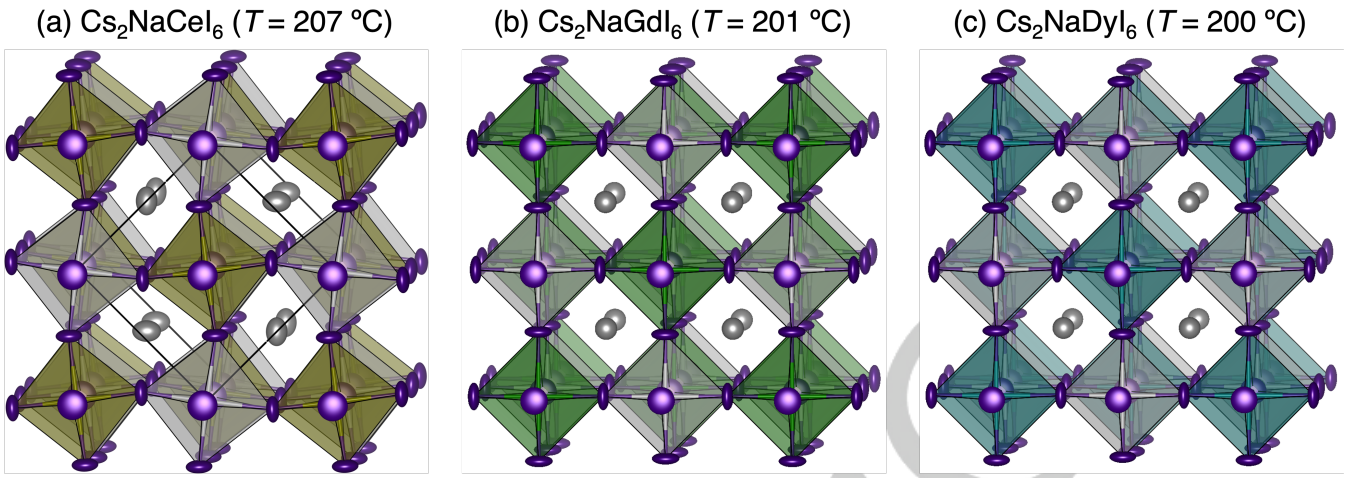


**Figure 1.** Single crystal X-ray structures of (a) $Cs_2NaCeI_6$, (b) $Cs_2NaGdI_6$, and (c) $Cs_2NaDyI_6$ drawn to scale, with respective data collection temperatures indicated. The atoms are shown as their thermal ellipsoids with 50% probabilities.

**Table 1.** Structural parameters of $Cs_2Na$*Ln*$I_6$ (*Ln* = Ce, Nd, Gd, Tb, Dy), from SC-XRD and DSC.

| Compound | Space group | Unit cell dimension (Å)[a] | Temperature (°C) | Cs–I distance (Å) | Ln–I distance (Å) | Na–I distance (Å) | Ln–Ln distance (Å) | Goldschmidt Tolerance Factor | Transition temperature to cubic phase (°C) |
|---|---|---|---|---|---|---|---|---|---|
| $Cs_2NaCeI_6$ | *P4/nmc* | 8.771(8)/ 12.514(11) | 207 | 4 × 4.386(4) 4 × 4.146(3) | 4 × 3.094(3) 2 × 3.096(3) | 4 × 3.155(3) 2 × 3.161(3) | 8.771(9) | 0.867 | ≈228[b] |
| $Cs_2NaNdI_6$ | *Fm*–3*m* | 12.386(4) | 202 | 4.379(1) | 3.055(2) | 3.138(2) | 8.758(3) | 0.870 | ≈200[a], 198[b] |
| $Cs_2NaGdI_6$ | *Fm*–3*m* | 12.28(1) | 201 | 4.343(3) | 3.008(3) | 3.134(3) | 8.685(8) | 0.876 | ≈150[a], 154[b] |
| $Cs_2NaTbI_6$ | *Fm*–3*m* | 12.268(5) | 200 | 4.337(1) | 3.003(2) | 3.131(3) | 8.675(4) | 0.878 | ≈135[a], 136[b] |
| $Cs_2NaDyI_6$ | *Fm*–3*m* | 12.23(1) | 200 | 4.323(4) | 2.978(3) | 3.135(3) | 8.644(8) | 0.880 | ≈120[a], 127[b] |

[a] Data derived from variable temperature SC-XRD. [b] Data derived from peak maxima of DSC traces.

anhydrous conditions (Supporting Information). Quenching the reaction tube with water was necessary to prevent any phase separation on cooling. In order to remove any persistent oxygen-containing impurities, the compounds were purified through a self-flux/transport method (details and photos in SI). This method affords high purity, crystalline materials that are free of any oxygen or binary salt-containing impurities, noting that these compounds are extremely sensitive to moisture and decompose instantly upon exposure to ambient air.

At room temperature, all compounds exhibited significant twinning and pseudosymmetry which made refinement of their single crystal structures very challenging. We were able to obtain a refinement of $Cs_2NaCeI_6$ in the monoclinic space group $P2_1/n$, while the remaining structures were unable to be refined at room temperature (Figure S1). Consistent with the room temperature single crystal X-ray diffraction (SC-XRD) findings, Pawley refinement with synchrotron X-ray powder diffraction data showed that all samples are best fit to the monoclinic space group $P2_1/n$ (Figure S2). The refinements also show a consistent decrease in lattice parameters and cell volumes with decreasing lanthanide ionic radius (Table S4). Upon heating the samples of $Cs_2Na$*Ln*$I_6$ to temperatures in the range 120 °C (*Ln* = Dy) to 202 °C (*Ln* = Nd), a phase transition to cubic *Fm*–3*m* is observed for *Ln* = Nd, Gd, Tb and Dy, allowing for determination of their single crystal structures (Figures 1 and S1).[30] Above these transition temperatures, the structures are analogous to the $K_2NaAlF_6$ elpasolite-type structure and exhibit corner-connected alternating sodium and lanthanide octahedra.[31] $Cs_2NaCeI_6$ is tetragonal (space group *P4/nmc*) at 207 °C, which was the highest temperature that we could reach on the single crystal X-ray diffractometer. Figure 1 shows the single crystal structures of $Cs_2NaCeI_6$, $Cs_2NaGdI_6$ and $Cs_2NaDyI_6$ as representatives of the $Cs_2Na$*Ln*$I_6$ series. The Ce–I bond distances in tetragonal $Cs_2NaCeI_6$ are 3.094(3) Å and 3.096(3) Å, while the Na–I bond distances are 3.161(3) Å and 3.155(3) Å. As required by the cubic symmetry of $Cs_2Na$*Ln*$I_6$ (*Ln* = Nd, Gd, Tb, Dy), there is only one *Ln*–I bond distance ranging from 3.055(2) Å (*Ln* = Nd) to 2.978(3) Å (*Ln* = Dy), and one Na–I bond distance, which ranges between 3.138(2) Å and 3.135(3) Å. A systematic decrease in the *Ln*–I bond distances follows the decrease of the ionic radius according to the lanthanide contraction, while the Na–I bond distances remain unchanged.[32] We observe that as the lanthanide ionic radius decreases, so does the transition temperature. This decrease in transition temperature follows the trend of increasing Goldschmidt tolerance factor on going from $Cs_2NaCeI_6$ to $Cs_2NaDyI_6$ (Table 1 and Figure S3). Differential scanning

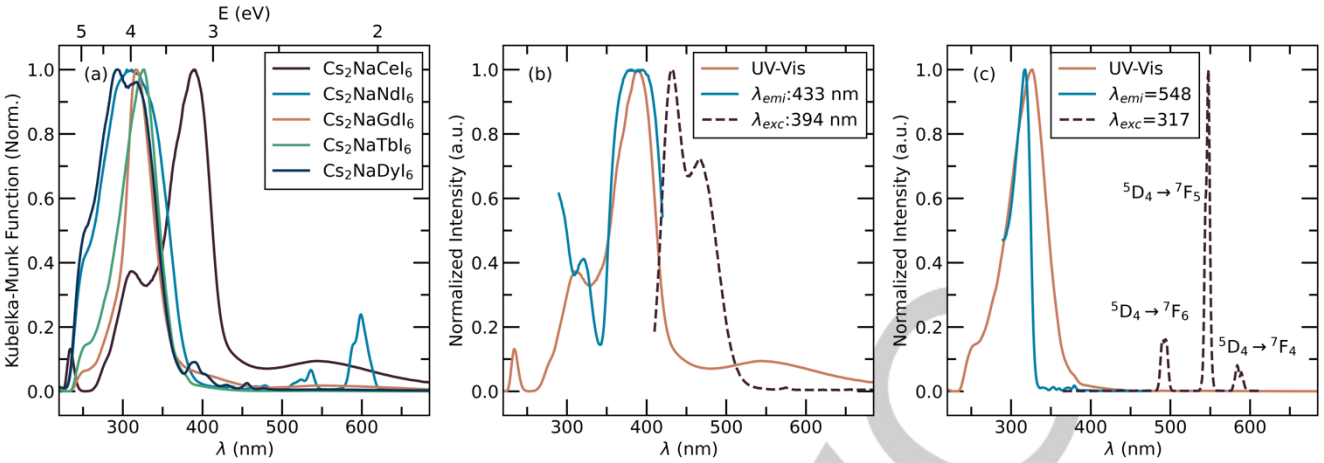


**Figure 2.** (a) UV–visible absorption spectra of iodide double perovskites $Cs_2NaLnI_6$ (*Ln* = Ce, Nd, Gd, Tb, Dy) recorded in diffuse reflectance mode and converted to absorbance by using the Kubelka-Munk function. (b) Normalized photoluminescent behaviour and absorption spectra of $Cs_2NaCeI_6$. (c) Normalized photoluminescent behaviour and absorption spectra of $Cs_2NaTbI_6$.

calorimetry (DSC) carried out on all compounds further confirms the trend of decreasing transition temperature with decreasing lanthanide ionic radius. Accordingly, DSC shows that the cubic transition temperature for $Cs_2NaCeI_6$ Is centered at 228 ºC and decreases to 127 ºC for $Cs_2NaDyI_6$ (Table 1 and Figure S4). Fitting the transition temperature *vs*. tolerance factor (from DSC) and extrapolating to room temperature suggests that a minimum tolerance factor of 0.894 would be required for a cubic structure (Figure S3), in excellent agreement with the literature prediction of $0.9<TF<1.0$.[33,34] For the $Cs_2NaM^{III}I_6$ composition, a $M^{III}$ cation would then require an ionic radius of <0.81 Å. In agreement with these results, Meyer and coworkers reported that $Cs_2NaScI_6$ ($Sc^{III}$ = 0.745 Å) displays cubic symmetry structure based on room temperature powder X-ray diffraction.[27] We also determined the coefficient of expansion for the cubic phases of $Cs_2NaLnI_6$ (*Ln* = Gd, Tb, Dy) above their transition temperatures by measuring the cubic lattice parameters in 10 ºC steps. All three phases exhibited almost zero thermal expansion (Figure S5), though the temperature ranges were quite limited. While positive thermal expansion is normally observed in iodide perovskites,[35] negative thermal expansion (NTE) has been noted in ordered $ReO_3$-type structures.[36,37]

The optical spectra of the $Cs_2NaLnI_6$ (*Ln* = Ce, Nd, Gd, Tb, Dy) family were measured using UV-Visible spectroscopy at room temperature (Figure 2a). All compounds show intense charge transfer (CT) behaviour. The absorption maxima between 290 and 320 nm can be attributed to iodide-based σ and π charge transfer to lanthanide 4f orbitals. The optical absorption edge energies of these compounds fall between 3.3 eV and 3.4 eV. The shoulder below 300 nm is also observed to increase in intensity following the increase in lanthanide reduction potential. For comparison, the CT bands in related chloride and bromide compounds are typically centered at higher energies around 200 nm and between 220 nm and 250 nm, respectively.[38–40] In the case of $Cs_2NaCeI_6$ a strong absorption centered at 390 nm can be assigned to the $^2F_{5/2}\rightarrow{}^2T_{2g}$ ($4f\rightarrow5d$) transition, while the absorbance centered at 310 nm is tentatively assigned as a CT band.

Given the well-known fluorescence of Ce(III), we next examined the photoluminescent properties of $Cs_2NaCeI_6$.[39,41,42] While monitoring at 433 nm, the excitation spectrum of $Cs_2NaCeI_6$ shows two absorptions centered at 321 nm (CT) and 394 nm ($^2F_{5/2}\rightarrow{}^2T_{2g}$) (Figure 2b). We suggest the rising shoulder below 310 nm arises from the $^2F_{5/2}\rightarrow{}^2E_g$ ($4f\rightarrow5d$) absorption, consistent with Ce(III) in the $M^{III}$ octahedral site.[28] For comparison, the excitation spectra of $Cs_2NaLaI_6$:2% Ce shows two 4f→5d excitations that are similar in position to $Cs_2NaCeI_6$, while the CT-based excitation is absent.[28] Upon excitation at 394 nm, a doublet emission profile with two peaks at 433 nm and 469 nm is observed, corresponding to the $^2T_{2g}\rightarrow{}^2F_{5/2}$ and $^2T_{2g}\rightarrow{}^2F_{7/2}$ transitions, respectively. This splitting of the $4f^1$ configuration into the $^2F_{7/2}$ and $^2F_{5/2}$ states is a result of spin-orbit coupling and is approximately independent of the ligand field strength.[39,40] Consequently, the energy difference between the $^2F_{5/2}$ and $^2F_{7/2}$ states (1773 $cm^{-1}$) is similar in energy to other cerium(III) emission profiles in a variety of host lattices and with varying ligands.[40,43] A Stokes shift of 2492 $cm^{-1}$ is similar to what has been previously observed in $Cs_2NaLaI_6$:2% Ce and $K_2LaI_5$:0.7% $Ce^{3+}$.[28,44] We note that the 4f→5d excitations and 5d→4f emissions are blue-shifted compared with the oxide phosphors that are used in solid state lighting,[45,46] presumably due to changes in the centroid shift and ligand field effects.[41] To further clarify the emission pathway, we also recorded the variable temperature emission spectra of $Cs_2NaCeI_6$ and determined the Huang-Rhys factor (*S*) and effective phonon energy ($\hbar\omega$) of the emissions centered at 433 nm and 469 nm (Figures S7 and S8), as described by others using equation S1.[47–49] As the temperature decreases, both emission features narrow, yielding $S = 9$ and $S = 28$ for the peaks at 433 nm and 469 nm, respectively, suggesting strong electron-phonon coupling.[47] These results are consistent with Ce(III) octahedra that are well separated,[50–52] due to the alternating Na octahedra. The increase in *S* between the two features is expected based on eq. S2. The effective phonon energies, 125 $cm^{-1}$ (433 nm) and $\hbar\omega$ = 111 $cm^{-1}$ (469 nm), are close in value and agree well with previously reported Ln–I Raman vibrational frequencies.[27,53]

Given the location of the CT band in the $Cs_2NaLnI_6$ series, we next sought to determine if excitation into the CT bands of $Cs_2NaTbI_6$ and $Cs_2NaDyI_6$ would result in energy transfer to a long lived 4f excited state that re-emits in the visible region. The emission spectra of $Cs_2NaTbI_6$ was acquired by exciting within the charge transfer band at 317 nm and shows an emission profile that is characteristic of a Tb(III) ion (Figure 2c).[54–57] Three sharp emission bands are located at 493 nm, 548 nm, and 584 nm, which are assigned to the $^5D_4 \rightarrow {}^7F_6$, $^5D_4 \rightarrow {}^7F_5$ and $^5D_4 \rightarrow {}^7F_4$ transitions of the Tb(III) ion. While exciting within the CT band of $Cs_2NaDyI_6$ ($\lambda_{ex}$ = 330 nm, Figure S6) we observe two characteristic $Dy^{3+}$ emission bands at 479 and 576 nm, corresponding to the $^4F_{9/2} \rightarrow {}^6H_{15/2}$ and $^4F_{9/2} \rightarrow {}^6H_{13/2}$ transitions, respectively.[58–60] The $^4I_{15/2} \rightarrow {}^6H_{15/2}$ and $^4I_{15/2} \rightarrow {}^6H_{13/2}$ emission bands are also observed at 456 and 545 nm, respectively, and are unusually intense.[58–60] While observation of luminesce from the $^4I_{15/2}$ state is not uncommon, [61] the intensities of these two emission bands are notably strong in relation to the $^4F_{9/2} \rightarrow {}^6H_{15/2}$ and $^4F_{9/2} \rightarrow {}^6H_{13/2}$ transitions.

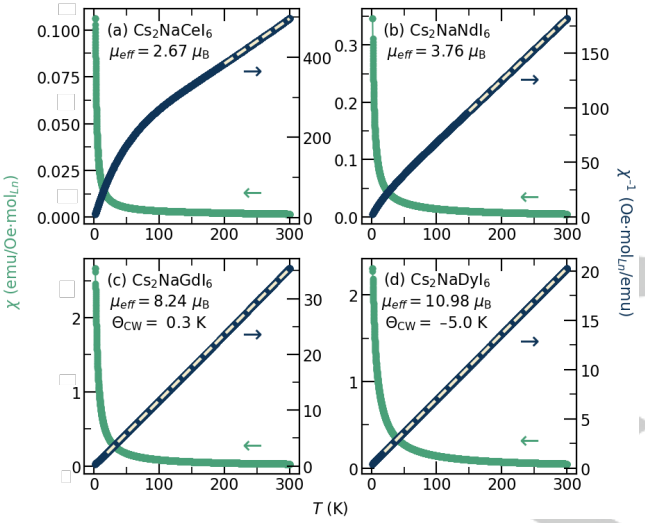


**Figure 3.** Magnetic susceptibility (left y-axis) and inverse magnetic susceptibility (right y-axis) plots of (a) $Cs_2NaCeI_6$ (b) $Cs_2NaNdI_6$, (c) $Cs_2NaGdI_6$, (d) $Cs_2NaDyI_6$ with Curie-Weiss fits (dashed line).

The magnetic susceptibilities of the entire $Cs_2NaLnI_6$ series were measured between $T$ = 2 K to 300 K and their Curie-Weiss fit parameters are summarized in Table S5. The long Ln–Ln distances and intervening $Na^+$ octahedra affords weakened coupling between magnetic ions, resulting in magnetic behaviour that is almost typical of the respective isolated trivalent lanthanide ion (Figures 3 and S9). In $Cs_2NaLnI_6$ (*Ln* = Ce, Nd), there is thermal depopulation of crystal field excited states at low temperatures, making determination of their $\theta_{cw}$ constants through the Curie-Weiss law meaningless (Figures 3a and 3b).[62] Fitting the Curie-Weiss law to the high temperature magnetic susceptibility data of $Cs_2NaCeI_6$ and $Cs_2NaNdI_6$ (*Ln* = Ce, $T$ > 200 K, *Ln* = Nd, $T$ > 150 K) yields room temperature moments of 2.67 $\mu_B$ per Ce and 3.76 $\mu_B$ per Nd, respectively. The room temperature moments of the entire $Cs_2NaLnI_6$ series all fall within 5% of their respective Russell-Saunders moments.[63] The agreement of the free-ion moments with the calculated moment underscores the high purity of these samples and also allows us to further observe the free ion effects for the entire series. In $Cs_2NaLnI_6$ (*Ln* = Tb, Dy) the crystal field splitting is much weaker than what is observed in $Cs_2NaCeI_6$ and $Cs_2NaNdI_6$, and Curie-Weiss behaviour is observed down to lower temperatures (Figures 3d and S9).[62] Ideal Curie-Weiss behaviour is obeyed by $Cs_2NaGdI_6$, due to $Gd^{3+}$ ($4f^7$) having no orbital (*L*) component contributing to the total angular momentum (Figure 3c). As insulating compounds with large inter rare-earth separations (Table 1), $Cs_2NaLnI_6$ (*Ln* = Gd, Tb, Dy) show relatively small $\theta_{cw}$ constants that are lower than the respective lanthanide oxide and chalcogenide materials (Table S5).[62,64–67] The Goodenough-Kanamori rules can be used to rationalize the slight tendencies towards antiferromagnetic ordering in both $Cs_2NaTbI_6$ ($\theta_{cw}$ = –4.7 K) and $Cs_2NaDyI_6$ ($\theta_{cw}$ = –5.0 K), while $Cs_2NaGdI_6$ shows almost no propensity to order ($\theta_{cw}$ = 0.3, Table S5).[68–70] Similar behaviour is also observed in the analogous chloride double perovskites $Cs_2NaLnCl_6$ (*Ln* = Ce, Nd, Tb, Dy).[71,72] The absence of magnetic ordering in $Cs_2NaGdI_6$ above 2 K and very small $\theta_{cw}$ constant, further driven by geometric magnetic frustration on the adopted fcc lattice,[73,74] suggests that this compound may also be an excellent candidate for low temperature magnetocaloric materials.[75–77]

To summarize, guided by a predictive model,[20] we have been able to synthesize and structurally characterize a family of iodide double perovskites using trivalent lanthanides. At high temperatures, the $Cs_2NaLnI_6$ (*Ln* = Ce, Nd, Gd, Tb, Dy) series adopts the cubic elpasolite structure, where the transition temperatures to the cubic structure decrease with decreasing lanthanide ionic radius and increasing Goldschmidt tolerance factor. The optical absorption edge energies of these compounds show the expected red shift compared with their chloride and bromide analogues, and the optical and magnetic properties have been studied in detail. Moving forward, we will investigate the use of organic cations in the *A* site and mixing the $M^{III}/M^{I}$ with other metals to enhance their air stability and conductive properties.

## Acknowledgements

This work was supported by the U. S. Department of Energy, Office of Science, Basic Energy Sciences, under DE-SC-0012541, and made use of shared facilities of the National Science Foundation (NSF) Materials Research Science and Engineering Center (MRSEC) at UC Santa Barbara (NSF DMR 1720256). A.K.C. thanks the Ras al Khaimah Centre for Advanced Materials for financial support. We also thank Dr. A. Mikhailovsky for help in collecting variable temperature PL data.

**Keywords:** Lanthanides • Iodide • Perovskite phases• Luminescence • Magnetism

[1] A. Kojima, K. Teshima, Y. Shirai, T. Miyasaka, *J. Am. Chem. Soc.* **2009**, *131*, 6050–6051.
[2] P. Gao, M. Grätzel, M. K. Nazeeruddin, *Energy Environ. Sci.* **2014**, *7*, 2448–2463.
[3] H.-S. Kim, C.-R. Lee, J.-H. Im, K.-B. Lee, T. Moehl, A. Marchioro, S.-J. Moon, R. Humphry-Baker, J.-H. Yum, J. E. Moser, M. Grätzel, N.-G. Park, *Sci Rep* **2012**, *2*, 591.
[4] M. M. Lee, J. Teuscher, T. Miyasaka, T. N. Murakami, H. J. Snaith, *Science* **2012**, *338*, 643–647.
[5] L. Etgar, P. Gao, Z. Xue, Q. Peng, A. K. Chandiran, B. Liu, Md. K. Nazeeruddin, M. Grätzel, *J. Am. Chem. Soc.* **2012**, *134*, 17396–17399.
[6] A. Al-Ashouri, E. Köhnen, B. Li, A. Magomedov, H. Hempel, P. Caprioglio, J. A. Márquez, A. B. Morales Vilches, E. Kasparavicius, J. A. Smith, N. Phung, D. Menzel, M. Grischek, L. Kegelmann, D. Skroblin, C. Gollwitzer, T. Malinauskas, M. Jošt, G. Matič, B. Rech, R.

Schlatmann, M. Topič, L. Korte, A. Abate, B. Stannowski, D. Neher, M. Stolterfoht, T. Unold, V. Getautis, S. Albrecht, *Science* **2020**, *370*, 1300–1309.
[7] F. Hao, C. C. Stoumpos, D. H. Cao, R. P. H. Chang, M. G. Kanatzidis, *Nat. Photon* **2014**, *8*, 489–494.
[8] A. H. Slavney, T. Hu, A. M. Lindenberg, H. I. Karunadasa, *J. Am. Chem. Soc.* **2016**, *138*, 2138–2141.
[9] F. Wei, Z. Deng, S. Sun, F. Zhang, D. M. Evans, G. Kieslich, S. Tominaka, M. A. Carpenter, J. Zhang, P. D. Bristowe, A. K. Cheetham, *Chem. Mater.* **2017**, *29*, 1089–1094.
[10] F. Giustino, H. J. Snaith, *ACS Energy Lett.* **2016**, *1*, 1233–1240.
[11] E. T. McClure, M. R. Ball, W. Windl, P. M. Woodward, *Chem. Mater.* **2016**, *28*, 1348–1354.
[12] F. Wei, Z. Deng, S. Sun, F. Xie, G. Kieslich, D. M. Evans, M. A. Carpenter, P. D. Bristowe, A. K. Cheetham, *Mater. Horiz.* **2016**, *3*, 328–332.
[13] Z. Deng, F. Wei, S. Sun, G. Kieslich, A. K. Cheetham, P. D. Bristowe, *J. Mater. Chem. A* **2016**, *4*, 12025–12029.
[14] S. E. Creutz, E. N. Crites, M. C. De Siena, D. R. Gamelin, *Nano Lett.* **2018**, *18*, 1118–1123.
[15] C. Zhang, L. Gao, S. Teo, Z. Guo, Z. Xu, S. Zhao, T. Ma, *Sustain. Energy Fuels* **2018**, *2*, 2419–2428.
[16] Y.-J. Li, T. Wu, L. Sun, R.-X. Yang, L. Jiang, P.-F. Cheng, Q.-Q. Hao, T.-J. Wang, R.-F. Lu, W.-Q. Deng, *RSC Adv.* **2017**, *7*, 35175–35180.
[17] P. Cheng, T. Wu, Y. Li, L. Jiang, W. Deng, K. Han, *New J. Chem.* **2017**, *41*, 9598–9601.
[18] A. J. Lehner, D. H. Fabini, H. A. Evans, C.-A. Hébert, S. R. Smock, J. Hu, H. Wang, J. W. Zwanziger, M. L. Chabinyc, R. Seshadri, *Chem. Mater.* **2015**, *27*, 7137–7148.
[19] P. Vishnoi, J. L. Zuo, T. A. Strom, G. Wu, S. D. Wilson, R. Seshadri, A. K. Cheetham, *Angew. Chem. Int. Ed.* **2020**, *59*, 8974–8981.
[20] P. Vishnoi, R. Seshadri, A. K. Cheetham, *J. Phys. Chem. C* **2021**, *125*, 11756–11764.
[21] M. E. Villafuerte-Castrejón, M. R. Estrada, J. Gómez-Lara, J. Duque, R. Pomés, *J. Solid State Chem* **1997**, *132*, 1–5.
[22] G. Meyer, S.-J. Hwu, J. D. Corbett, *Z Anorg Allg Chem* **1986**, *535*, 208–212.
[23] V. Poblete, G. Navarro, V. Martin, M. Alvarez, *Powder Diffr.* **2002**, *17*, 10–12.
[24] M. S. Wickleder, G. Meyer, *Z Anorg Allg Chem* **1995**, *621*, 457–463.
[25] L. R. Morss, M. Siegal, L. Stenger, N. Edelstein, *Inorg. Chem.* **1970**, *9*, 1771–1775.
[26] Z. Deng, F. Wei, F. Brivio, Y. Wu, S. Sun, P. D. Bristowe, A. K. Cheetham, *J. Phys. Chem. Lett.* **2017**, *8*, 5015–5020.
[27] G. Meyer, *Z. Naturforsch. B* **1980**, *35*, 394–396.
[28] G. Gundiah, K. Brennan, Z. Yan, E. C. Samulon, G. Wu, G. A. Bizarri, S. E. Derenzo, E. D. Bourret-Courchesne, *J. Lumin.* **2014**, *149*, 374–384.
[29] P. Yang, F. P. Doty, M. A. Rodriguez, M. R. Sanchez, X. Zhou, K. S. Shah, *Mater Res Soc Symp Proc* **2009**, *1164*, 1164-L11-05.
[30] Deposition numbers 2250567 and 2250566 (for $Cs_2NaCeI_6$), 2250563 (for $Cs_2NaNdI_6$), 2250562 and 2256784(for $Cs_2NaGdI_6$), 2250564 and 2256782 (for $Cs_2NaTbI_6$), and 2250565 and 2256783 (for $Cs_2NaDyI_6$) contain the supplementary crystallographic data for this paper. These data are provided free of charge by the joint Cambridge Crystallographic Data Centre and Fachinformationszentrum Karlsruhe.
[31] L. R. Moras, *J. Inorg. Nucl. Chem.* **1974**, *36*, 3876–3878.
[32] R. D. Shannon, *Acta Cryst A* **1976**, *32*, 751–767.
[33] G. Kieslich, S. Sun, A. K. Cheetham, *Chem. Sci.* **2014**, *5*, 4712–4715.
[34] Z. Li, M. Yang, J.-S. Park, S.-H. Wei, J. J. Berry, K. Zhu, *Chem. Mater.* **2016**, *28*, 284–292.
[35] D. H. Fabini, C. C. Stoumpos, G. Laurita, A. Kaltzoglou, A. G. Kontos, P. Falaras, M. G. Kanatzidis, R. Seshadri, *Angew. Chem. Int. Ed* **2016**, *55*, 15392–15396.
[36] J. C. Hancock, K. W. Chapman, G. J. Halder, C. R. Morelock, B. S. Kaplan, L. C. Gallington, A. Bongiorno, C. Han, S. Zhou, A. P. Wilkinson, *Chem. Mater.* **2015**, *27*, 3912–3918.
[37] H. A. Evans, Y. Wu, R. Seshadri, A. K. Cheetham, *Nat. Rev. Mater.* **2020**, *5*, 196–213.
[38] P. J. Dereń, W. Stręk, J.-C. Krupa, *Chem. Phys. Lett* **1998**, *298*, 217–221.
[39] K. W. Krämer, P. Dorenbos, H. U. Güdel, C. W. E. van Eijk, *J. Mater. Chem.* **2006**, *16*, 2773–2780.
[40] O. Guillot-Noël, J. T. M. de Haas, P. Dorenbos, C. W. E. van Eijk, K. Krämer, H. U. Güdel, *J. Lumin.* **1999**, *85*, 21–35.
[41] P. Dorenbos, *Phys. Rev. B* **2001**, *64*, 125117.
[42] A. Bessière, P. Dorenbos, C. W. E. van Eijk, L. Pidol, K. W. Krämer, H. U. Güdel, *J. Phys.: Condens. Matter* **2004**, *16*, 1887.
[43] E. V. D. van Loef, P. Dorenbos, C. W. E. van Eijk, K. W. Krämer, H. U. Güdel, *Phys. Rev. B* **2003**, *68*, 045108.
[44] E. V. D. van Loef, P. Dorenbos, C. W. E. van Eijk, K. W. Krämer, H. U. Güdel, *Nucl. Instrum. Methods Phys. Res.* **2005**, *537*, 232–236.
[45] J. L. Wu, G. Gundiah, A. K. Cheetham, *Chem. Phys. Lett.* **2007**, *441*, 250–254.
[46] N. C. George, K. A. Denault, R. Seshadri, *Annu. Rev. Mater. Res.* **2013**, *43*, 481–501.
[47] K. Huang, B. Zhu, *Selected Papers of Kun Huang: With Commentary*, World Scientific, **2000**.
[48] K. Xu, Q. Wei, H. Wang, B. Yao, W. Zhou, R. Gao, H. Chen, H. Li, J. Wang, Z. Ning, *Nanoscale* **2022**, *14*, 2248–2255.
[49] K. M. McCall, C. C. Stoumpos, S. S. Kostina, M. G. Kanatzidis, B. W. Wessels, *Chem. Mater.* **2017**, *29*, 4129–4145.
[50] D. W. Cooke, B. L. Bennett, K. J. McClellan, J. M. Roper, M. T. Whittaker, *J. Appl. Phys.* **2000**, *87*, 7793–7797.
[51] J. He, R. Shi, M. G. Brik, P. Dorenbos, Y. Huang, Y. Tao, H. Liang, *J. Lumin.* **2015**, *161*, 257–263.
[52] Y. Ou, W. Zhou, D. Hou, M. G. Brik, P. Dorenbos, Y. Huang, H. Liang, *RSC Adv.* **2019**, *9*, 7908–7915.
[53] M. M. Metallinou, L. Nalbandian, G. N. Papatheodorou, W. Voigt, H. H. Emons, *Inorg. Chem.* **1991**, *30*, 4260–4264.
[54] L. Beauzamy, B. Moine, P. Gredin, *J. Lumin.* **2007**, *127*, 568–574.
[55] Y. Liu, X. Rong, M. Li, M. S. Molokeev, J. Zhao, Z. Xia, *Angew. Chem. Int. Ed.* **2020**, *59*, 11634–11640.
[56] G. Ju, Y. Hu, L. Chen, X. Wang, L. Hung, *Appl. Phys. A* **2014**, *114*, 867–874.
[57] C. S. McCaw, K. M. Murdoch, R. G. Denning, *Mol. Phys* **2003**, *101*, 427–438.
[58] W. T. Carnall, P. R. Fields, K. Rajnak, *J. Chem. Phys.* **1968**, *49*, 4424–4442.
[59] W. T. Carnall, G. L. Goodman, K. Rajnak, R. S. Rana, *J. Chem. Phys.* **1989**, *90*, 3443–3457.
[60] N. Kofod, R. Arppe-Tabbara, T. J. Sørensen, *J. Phys. Chem. A* **2019**, *123*, 2734–2744.
[61] Ž. Antić, M. D. Dramićanin, K. Prashanthi, D. Jovanović, S. Kuzman, T. Thundat, *Adv. Mater.* **2016**, *28*, 7745–7752.
[62] S. Mugiraneza, A. M. Hallas, *Commun Phys* **2022**, *5*, 95.
[63] R. L. Carlin, *Magnetochemistry*, Springer Science & Business Media, **1986**.
[64] G. Morrison, H.-C. zur Loye, *J. Solid State Chem.* **2015**, *221*, 334–337.
[65] B. R. Ortiz, M. M. Bordelon, P. Bhattacharyya, G. Pokharel, P. M. Sarte, L. Posthuma, T. Petersen, M. S. Eldeeb, G. E. Granroth, C. R. Dela Cruz, S. Calder, D. L. Abernathy, L. Hozoi, S. D. Wilson, *Phys. Rev. Mater.* **2022**, *6*, 084402.
[66] P. Veber, M. Velázquez, G. Gadret, D. Rytz, M. Peltz, R. Decourt, *CrystEngComm* **2015**, *17*, 492–497.
[67] W. Liu, Z. Zhang, J. Ji, Y. Liu, J. Li, X. Wang, H. Lei, G. Chen, Q. Zhang, *Chin. Phys. Lett.* **2018**, *35*, 117501.
[68] J. B. Goodenough, *J. Phys. Chem. Solids* **1958**, *6*, 287–297.
[69] J. B. Goodenough, *Phys. Rev.* **1955**, *100*, 564–573.
[70] J. Kanamori, *J. Phys. Chem. Solids* **1959**, *10*, 87–98.
[71] F. W. Voss, R. Nevald, I. Laursen, H.-D. Amberger, *J. Less-Common Met.* **1983**, *94*, 233–241.
[72] M. V. Hoehn, D. G. Karraker, *J. Chem. Phys.* **1974**, *60*, 393–397.
[73] H. Karunadasa, Q. Huang, B. G. Ueland, P. Schiffer, R. J. Cava, *Proc. Natl. Acad. Sci. U.S.A.* **2003**, *100*, 8097–8102.
[74] G. Chen, R. Pereira, L. Balents, *Phys. Rev. B* **2010**, *82*, 174440.
[75] R. Sessoli, *Angew. Chem., Int. Ed.* **2012**, *51*, 43–45.
[76] Y.-C. Chen, F.-S. Guo, Y.-Z. Zheng, J.-L. Liu, J.-D. Leng, R. Tarasenko, M. Orendáč, J. Prokleška, V. Sechovský, M.-L. Tong, *Chem. Eur. J* **2013**, *19*, 13504–13510.
[77] A. V. Pavlishchuk, V. V. Pavlishchuk, *Theor. Exp. Chem.* **2020**, *56*, 1–25.

## Entry for the Table of Contents

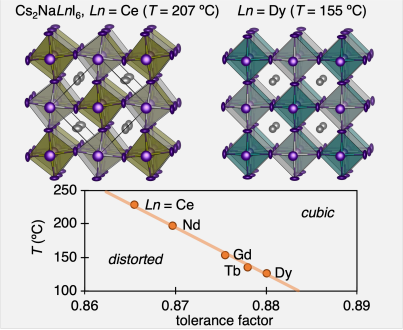


Unicorn double perovskite iodides [$A_2M^{I}M^{III}I_6$] are elusive, but with the help of rational design rules, can indeed be synthesized. The $Cs_2NaLnI_6$ (*Ln* = Ce, Nd, Gd, Tb, Dy) family demonstrate optical properties that are red shifted compared to related halide materials and their magnetic properties show weak interaction parameters.

**Supporting information for:**

# Elusive Double Perovskite Iodides: Structural, Optical, and Magnetic Properties

Greggory T. Kent[a], Emily Morgan[a], Kaitlin R. Albanese[a][b], Anna Kallistova[a], Alexandra Brumberg[a], Linus Kautzsch[a], Guang Wu[b], Pratap Vishnoi[c], Ram Seshadri*[a] and Anthony K. Cheetham*[a][d]

[a] Materials Department and Materials Research Laboratory, University of California, Santa Barbara, CA 93106 (USA)
[b] Department of Chemistry and Biochemistry, University of California, Santa Barbara, CA 93106 (USA)
[c] New Chemistry Unit and International Centre for Materials Science, Jawaharlal Nehru Centre for Advanced Scientific Research (JNCASR), Bangalore 560064 (India)
[d] Department of Materials Science & Engineering, National University of Singapore, 117576 Singapore (Singapore)

*To whom correspondence should be addressed. Email: seshadri@mrl.ucsb.edu and akc30@cam.ac.uk

## Table of Contents

## Experimental

**General.** All reactions and subsequent manipulations were performed under strictly anaerobic and anhydrous conditions under an atmosphere of argon. All reagents were purchased from commercial vendors as anhydrous salts and used as received.

**Magnetic Measurments.** The magnetic properties of all compounds were recorded using a Quantum Design Magnetic Property Measurement System SQUID vibrating sample magnetometer (MPMS3 SQUID-VSM). All powdered samples were loaded in plastic caps under an inert atmosphere and mounted on a brass holder for measurements. Zero-field cooled and field cooled measurements were taken on warming from 2K to 300K under a constant field of 1 Tesla.

**Optical properties.** Diffuse reflectance spectra were collected on a Shimadzu UV-3600 UV–vis–NIR spectrometer using $BaSO_4$ (Sigma Aldrich) as the reference for 100% reflectance. The spectra were collected by adding powdered samples, diluted with $BaSO_4$, to a sample holder and applying transparent tape over the samples to prevent decomposition from air. The diffuse reflectance data were transformed into the absorbance by using the Kubelka–Munk (K-M) expression. Steady-state photoluminescent data were obtained using a Jobin-Yvon HORIBA FluoroMax-4 (xenon source, 2.3 nm excitation and emission slit widths, 1 nm step size) equipped with a solid-state sample holder. Fluorescence spectra were also collected by adding powdered samples, diluted with $BaSO_4$, to a sample holder and applying transparent tape over the samples to prevent decomposition from air. Photoluminescent data were analyzed using the FluorEssence (v3.5) software powered by Origin.

The temperature-dependent steady state photoluminescence (PL) measurements were performed on a home-built fluorometer setup. The PL was excited by a solid state laser beam (Coherent OBIS) with 375 nm wavelength at 45 degrees angle of incidence. The incident beam power was <500 uW focused into the spot with a Gaussian diameter of ~100um. The PL was collected in 90 degrees geometry with an optical lens system and focused on the input slit of a spectrometer (Acton SP-500) equipped with a charge-coupled device (CCD) camera (Princeton Instruments PIXIS:400) which can detect light in the range 300-1050 nm. The CCD detector was protected from the excitation light by a long-pass interference filter (Omega Filters ALP400). The spectrum, collected by the CCD camera, was corrected for the instrument response by measuring the spectrum of a

black body-like light source (Ocean Optics HL-1) and calculating the appropriate correction factor. To control the temperature, the sample was placed into an LN2-cooled cryostat (Janis VPF-100 with Thermaltake 323 controller). The spectra were processed and fit using the Fityk software package.

**Differential Scanning Calorimetry.** Differential Scanning Calorimetry (DSC) was performed using a TA Instruments DSC Q2000 at a heating/cooling rate of 10 °C/min using 3–5 mg of sample in a sealed aluminum pan.

**Synchrotron X-ray diffraction and Pawley refinements.** High-resolution synchrotron powder X-ray diffraction data were collected at beamline 11-BM at the Advanced Photon Source at Argonne National Laboratory. Samples were flame sealed in 1 mm glass capillaries and nested in Kapton tubes. The presence of LnOI in some samples is a result of issues with advantageous air when sealing capillaries and was not observed in laboratory X-ray diffraction studies. The powder X-ray diffraction data were analyzed using the TOPAS software suite.[1] Pawley refinements were performed to determine Space groups and lattice parameters.

**Single Crystal X-ray Crystallography.** Data for all compounds $Cs_2NaLnI_6$ (Ln = Ce, Nd, Gd, Tb, Dy) were collected on a Bruker KAPPA APEX II diffractometer equipped with an APEX II CCD detector using a TRIUMPH monochromater with a Mo Kα X-ray source (α = 0.71073 Å). The crystals were mounted on a quartz rod under Paratone-N oil, and data were collected at 428(2) K, where Ln = Gd, Tb, and Dy, 475(2) K for $Cs_2NaLnI_6$ (Ln = Nd, Gd, Tb, and Dy), and 480(2)/298(2) K for $Cs_2NaCeI_6$ using an Oxford nitrogen gas cryostream system. X-ray data for $Cs_2NaLnI_6$ (Ln = Ce, Nd, Gd, Tb, Dy)were collected utilizing frame exposures of 20 s. Data collection and cell parameter determination were conducted using the SMART program.[2] Integration of the data frames and final cell parameter refinement were performed using SAINT software.[3] Absorption corrections of the data were carried out using the multi-scan method SADABS.[4] Subsequent calculations were carried out using SHELXTL.[5] Structure determination was done using direct or Patterson methods and difference Fourier techniques. Structure solution, refinement, graphics, and creation of publication materials were performed using SHELXTL.[5]

Further crystallographic details can be found in Tables S1 S2 and S3. Compounds $Cs_2NaLnI_6$ (Ln = Ce, Nd, Gd, Tb, Dy) have been deposited in the Cambridge Structural Database ($Cs_2NaCeI_6$-RT: CCDC 2250566; $Cs_2NaCeI_6$-HT: CCDC 2250567; $Cs_2NaNdI_6$: CCDC 2250563; $Cs_2NaGdI_6$: CCDC 2250562 and 2256784-HT; $Cs_2NaTbI_6$: CCDC 2250564 and 2256782-HT; $Cs_2NaDyI_6$: 2250565 and 2256783-HT).

**Synthesis.** In a typical synthesis, stoichiometric quantities of 2 equivalents CsI, 1 equivalent NaI and 1 equivalent $LnI_3$ were weighed in an argon glovebox with oxygen and water levels of <0.5 ppm. These materials were ground and pressed into a pellet that was then loaded into an alumina crucible inside a silica tube. The reaction tube was sealed under vacuum and heated to 675 ºC. After heating for 16 h the reaction tube was quenched with room temperature water, dried and brought back into the glovebox. Depending on the purity of the lanthanide iodide salt, the resulting powders were often contaminated with impurities that could be removed with a self-flux/transport. In a typical purification step, the crude powder was charged into a silica tube and sealed under vacuum at a length of 9". Heating one end of the tube to 725 ºC, with the other end sticking out of the tube furnace for 24 h resulted in transport of the desired material towards the cool end. Lanthanide containing impurities remained at the hot end while any iodine (from decomposition) and binary salts could be found at the cool end (Figure S11). The reaction tube was quenched with room temperature water yielding a highly crystalline product (Figure S10).

**Table S1**. X-ray Crystallographic Data for Compounds $Cs_2NaCeI_6$, and $Cs_2NaNdI_6$.

| | $Cs_2NaCeI_6$-RT | $Cs_2NaCeI_6$-HT | $Cs_2NaNdI_6$ |
|---|---|---|---|
| empirical formula | $Cs_2NaCeI_6$ | $Cs_2NaCeI_6$ | $Cs_2NaNdI_6$ |
| Crystal habit, color | Block, Light-yellow | Block, Light-yellow | Block, Light-blue |
| crystal size (mm) | 0.15 × 0.10 × 0.05 | 0.15 × 0.15 × 0.10 | 0.20 × 0.20 × 0.15 |
| crystal system | Monoclinic | Tetragonal | Cubic |
| space group | $P2_1/n$ | P4/mnc | Fm–3m |
| vol ($Å^3$) | 922.8(5) | 962.8(19) | 1900.4(19) |
| a (Å) | 8.594(3) | 8.771(8) | 12.386(4) |
| b (Å) | 8.691(3) | 8.771(8) | 12.386(4) |
| c (Å) | 12.354(4) | 12.51(1) | 12.386(4) |
| α (deg) | 90 | 90 | 90 |
| β (deg) | 90.27(3) | 90 | 90 |
| γ (deg) | 90 | 90 | 90 |
| Z | 2 | 2 | 4 |
| T (K) | 298(2) | 480(2) | 475(2) |
| fw (g/mol) | 1190.33 | 1190.33 | 1194.45 |
| density (calcd) ($Mg/m^3$) | 4.284 | 4.106 | 4.175 |
| abs coeff ($mm^{-1}$) | 16.376 | 15.695 | 16.240 |
| $F_{000}$ | 994 | 994 | 1996 |
| Total no. reflections | 1936 | 533 | 143 |
| Unique reflections | 1328 | 380 | 130 |
| $R_{int}$ | 0.0569 | 0.0379 | 0.0241 |
| final R indices [$I > 2\sigma(I)$] | $R_1 = 0.0706$, $wR_2 = 0.1649$ | $R_1 = 0.0435$, $wR_2 = 0.1055$ | $R_1 = 0.0328$, $wR_2 = 0.0572$ |
| largest diff peak and hole ($e^-Å^{-3}$) | 2.070 and -2.135 | 1.152 and -1.204 | 0.724 and -1.037 |
| GOF | 1.102 | 1.051 | 1.097 |

**Table S2**. X-ray Crystallographic Data for Compounds $Cs_2NaGdI_6$, $Cs_2NaTbI_6$, and $Cs_2NaDyI_6$ at 155ºC.

| | $Cs_2NaGdI_6$ | $Cs_2NaTbI_6$ | $Cs_2NaDyI_6$ |
|---|---|---|---|
| empirical formula | $Cs_2NaGdI_6$ | $Cs_2NaTbI_6$ | $Cs_2NaDyI_6$ |
| Crystal habit, color | Block, Colorless | Block, Colorless | Block, Colorless |
| crystal size (mm) | 0.15 × 0.1× 0.05 | 0.10 × 0.10 × 0.10 | 0.10 × 0.10 × 0.075 |
| crystal system | Cubic | Cubic | Cubic |
| space group | Fm–3m | Fm–3m | Fm–3m |
| vol ($Å^3$) | 1848(3) | 1837(5) | 1787(4) |
| a (Å) | 12.272(6) | 12.25 (1) | 12.135(9) |
| b (Å) | 12.272(6) | 12.25(1) | 12.135(9) |
| c (Å) | 12.272(6) | 12.25(1) | 12.135(9) |
| α (deg) | 90 | 90 | 90 |
| β (deg) | 90 | 90 | 90 |
| γ (deg) | 90 | 90 | 90 |
| Z | 4 | 4 | 4 |
| T (K) | 428(2) | 428(2) | 428(2) |
| fw (g/mol) | 1207.46 | 1209.13 | 1212.71 |
| density (calcd) ($Mg/m^3$) | 4.339 | 4.372 | 4.508 |
| abs coeff ($mm^{-1}$) | 17.477 | 17.824 | 18.547 |
| $F_{000}$ | 2012 | 2016 | 2020 |
| Total no. reflections | 111 | 129 | 128 |
| Unique reflections | 91 | 114 | 96 |
| $R_{int}$ | 0.0453 | 0.0468 | 0.0718 |
| final R indices [$I > 2\sigma(I)$] | $R_1$ = 0.0424, $wR_2$ = 0.0924 | $R_1$ = 0.0323, $wR_2$ = 0.0535 | $R_1$ = 0.0369, $wR_2$ = 0.0568 |
| largest diff peak and hole ($e^-Å^{-3}$) | 0.913 and -0.819 | 0.606 and -0.769 | 1.241and -1.607 |
| GOF | 1.073 | 1.167 | 1.333 |

**Table S3**. X-ray Crystallographic Data for Compounds $Cs_2NaGdI_6$, $Cs_2NaTbI_6$, and $Cs_2NaDyI_6$ at 200ºC.

| | $Cs_2NaGdI_6$ | $Cs_2NaTbI_6$ | $Cs_2NaDyI_6$ |
|---|---|---|---|
| empirical formula | $Cs_2NaGdI_6$ | $Cs_2NaTbI_6$ | $Cs_2NaDyI_6$ |
| Crystal habit, color | Block, Colorless | Block, Colorless | Block, Colorless |
| crystal size (mm) | 0.15 × 0.10 × 0.10 | 0.15 × 0.15 × 0.10 | 0.20 × 0.10 × 0.05 |
| crystal system | Cubic | Cubic | Cubic |
| space group | Fm–3m | Fm–3m | Fm–3m |
| vol ($Å^3$) | 1853(4) | 1846(2) | 1827(5) |
| a (Å) | 12.28 (1) | 12.268(5) | 12.23(1) |
| b (Å) | 12.28 (1) | 12.268(5) | 12.23(1) |
| c (Å) | 12.28 (1) | 12.268(5) | 12.23(1) |
| α (deg) | 90 | 90 | 90 |
| β (deg) | 90 | 90 | 90 |
| γ (deg) | 90 | 90 | 90 |
| Z | 4 | 4 | 4 |
| T (K) | 474(2) | 473(2) | 473(2) |
| fw (g/mol) | 1207.46 | 1209.13 | 1212.71 |
| density (calcd) ($Mg/m^3$) | 4.327 | 4.350 | 4.409 |
| abs coeff ($mm^{-1}$) | 17.429 | 17.734 | 18.140 |
| $F_{000}$ | 2012 | 2016 | 2020 |
| Total no. reflections | 131 | 131 | 128 |
| Unique reflections | 116 | 114 | 103 |
| $R_{int}$ | 0.0260 | 0.0961 | 0.0430 |
| final R indices [$I > 2\sigma(I)$] | $R_1$ = 0.0291, $wR_2$ = 0.1020 | $R_1$ = 0.0527, $wR_2$ = 0.1512 | $R_1$ = 0.0289, $wR_2$ = 0.0351 |
| largest diff peak and hole ($e^-Å^{-3}$) | 0.625 and -0.780 | 1.480 and -3.192 | 0.952 and -0.871 |
| GOF | 1.051 | 1.039 | 1.163 |

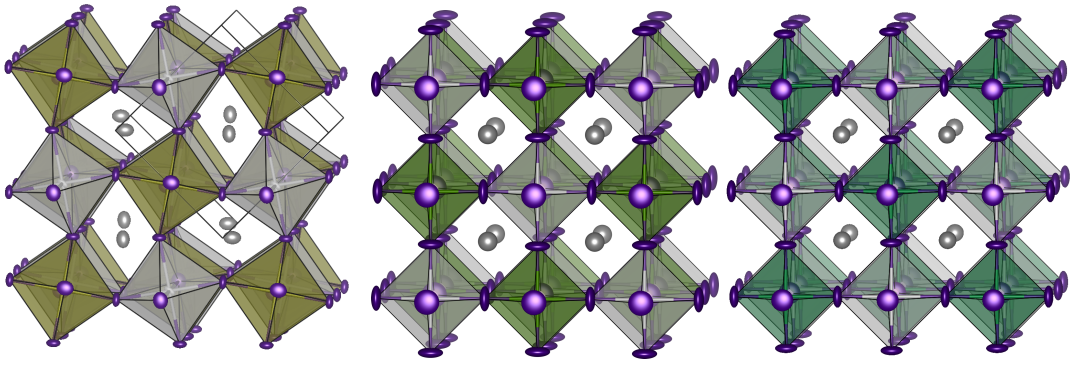

**Figure S1.** Single crystal X-ray structures of $Cs_2NaCeI_6$ (left, 298 K) $Cs_2NaNdI_6$ (middle, 475 K) and $Cs_2NaTbI_6$ (right, 473 K), the thermal ellipsoids of all atoms are shown at their 50% probabilities.

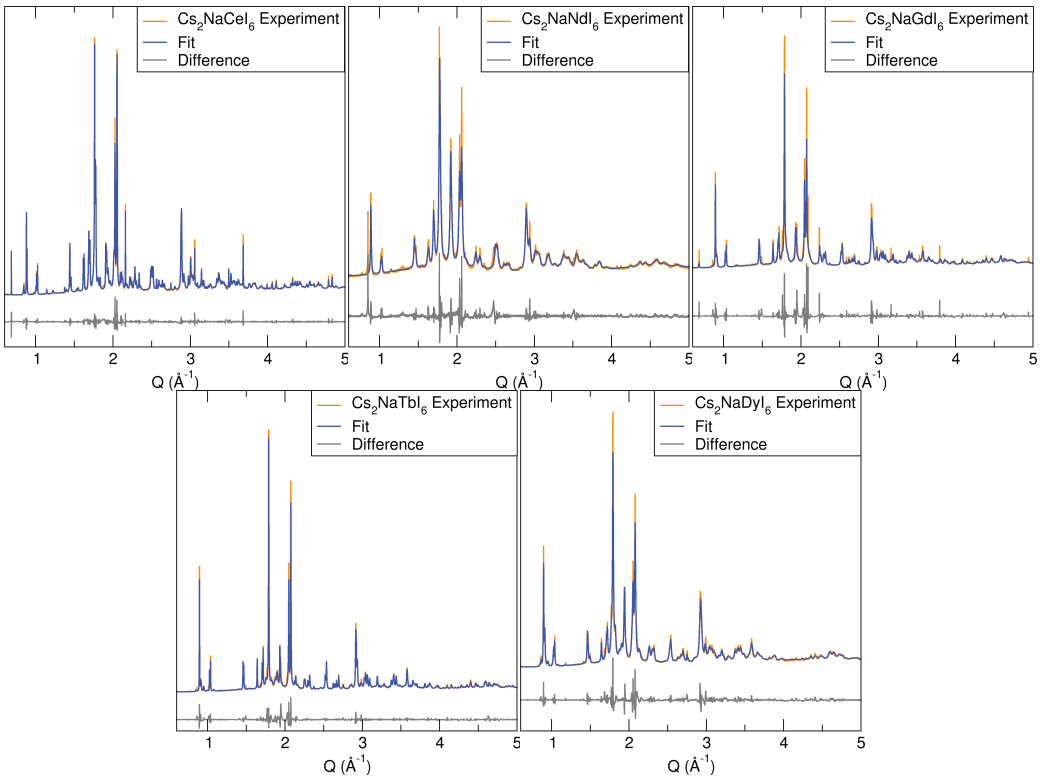


**Figure S2.** 11-BM synchrotron X-ray diffraction data, fit, and difference for $Cs_2NaLnI_6$ (*Ln* = Ce, Nd, Gd, Tb, Dy).

**Table S4.** Lattice Parameters determined from Pawley refinement.

| empirical formula | $Cs_2NaCeI_6$ | $Cs_2NaNdI_6$ | $Cs_2NaGdI_6$ | $Cs_2NaTbI_6$ | $Cs_2NaDyI_6$ |
|---|---|---|---|---|---|
| crystal system | Monoclinic | Monoclinic | Monoclinic | Monoclinic | Monoclinic |
| space group | $P2_1/n$ | $P2_1/n$ | $P2_1/n$ | $P2_1/n$ | $P2_1/n$ |
| vol (Å$^3$) | 930.28(2) | 915.0(1) | 899.1(1) | 898.42(4) | 893.48(8) |
| a (Å) | 8.61526(9) | 8.552(1) | 8.5587(6) | 8.5544(2) | 8.5408(5) |
| b (Å) | 8.70888(8) | 8.669(9) | 8.5630(6) | 8.5654(2) | 8.5444(5) |
| c (Å) | 12.3989(1) | 12.347(1) | 12.2681(6) | 12.2614(2) | 12.2437(5) |
| α (deg) | 90 | 90 | 90 | 90 | 90 |
| β (deg) | 90.2061(7) | 90.531(7) | 90.257(6) | 90.148(2) | 90.353(8) |
| γ (deg) | 90 | 90 | 90 | 90 | 90 |
| $R_{wp}$ | 5.53% | 8.00% | 12.66% | 8.72% | 7.95% |
| $R_p$ | 4.09% | 5.83% | 9.18% | 6.26% | 6.32% |

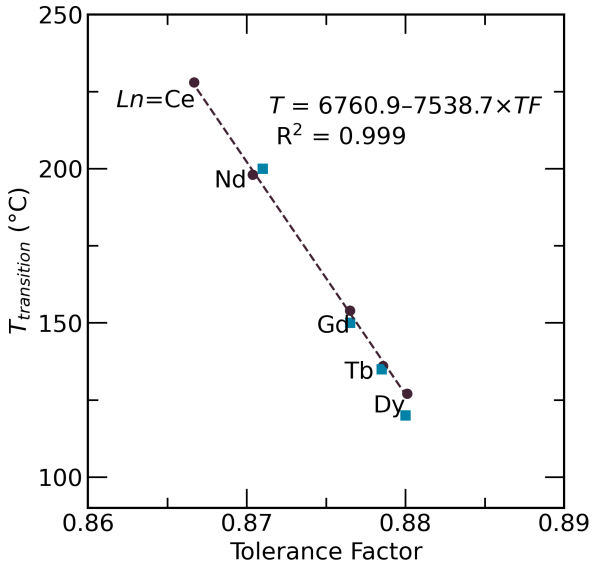


**Figure S3.** Plot showing tolerance factor vs transition temperature to cubic for $Cs_2NaLnI_6$ (Ln = Ce, Nd, Gd, Tb, Dy) using SC-XRD (squares) and DSC (circles); linear fit uses DSC data.

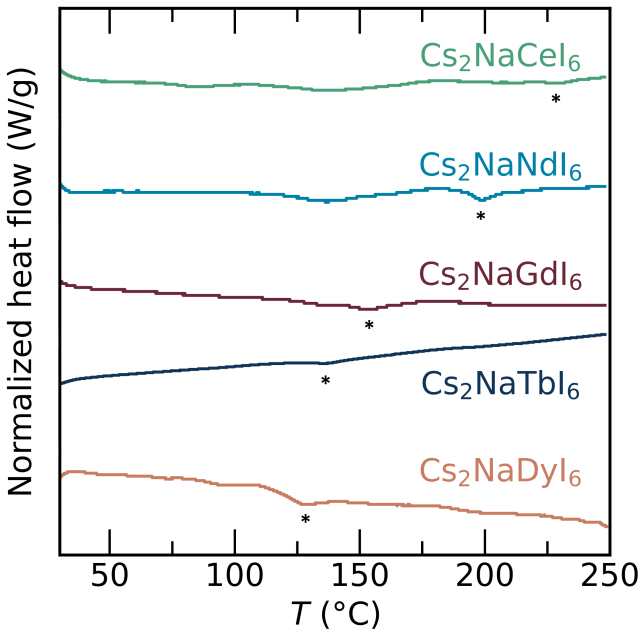


**Figure S4.** DSC thermograms of $Cs_2NaLnI_6$ (Ln = Ce, Nd, Gd, Tb, Dy). The second heat, with a ramp rate of 10 °C $min^{-1}$, is plotted for clarity and with exotherm up. The cubic transition temperature, denoted with (*), of $Cs_2NaLnI_6$ is the predominant thermal feature in each DSC trace.

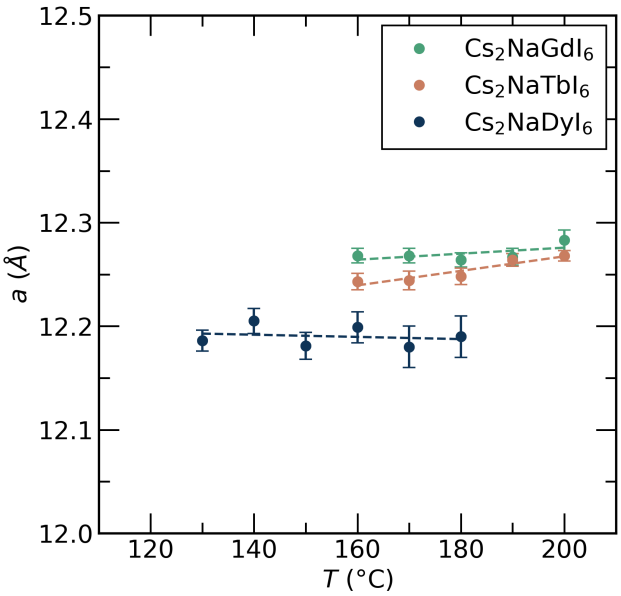


**Figure S5.** SC-XRD cubic phase lattice parameter plotted as a function of temperature for $Cs_2NaLnI_6$ (Ln = Gd, Tb, Dy) with error bars set at 1σ. Dashed lines are linear fits used to guide the eye.

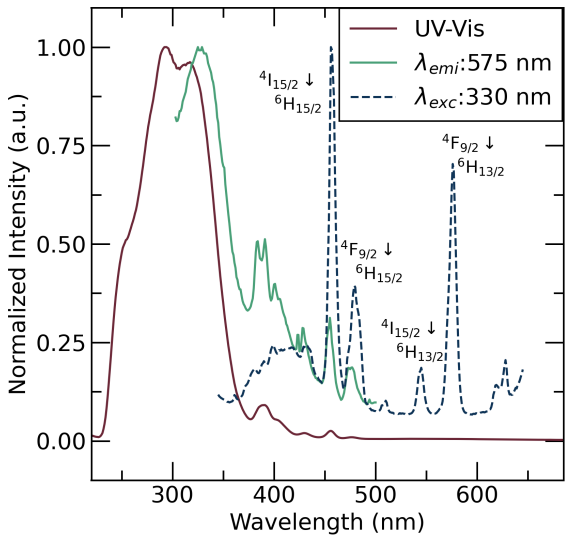


**Figure S6.** Normalized excitation, emission, and UV-Vis spectra of $Cs_2NaDyI_6$ taken at room temperature.

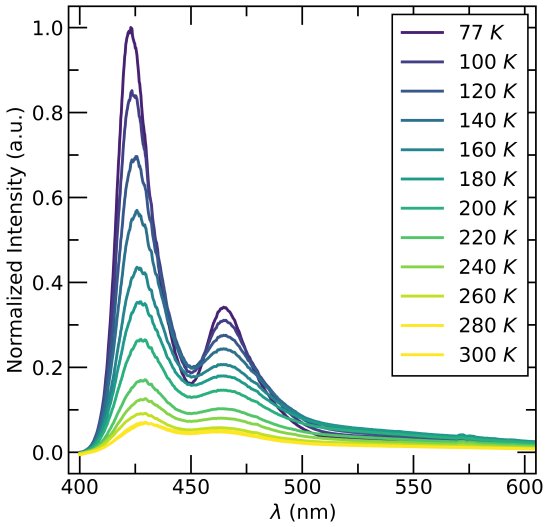


**Figure S7.** Variable temperature emission spectra of $Cs_2NaCeI_6$, measured while exciting at 375 nm.

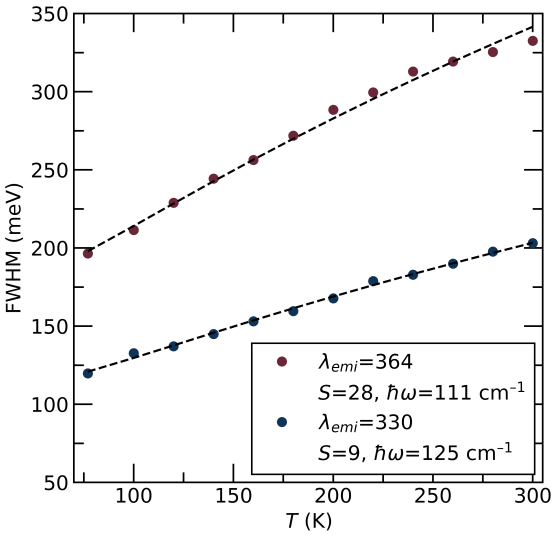


**Figure S8.** Temperature-dependent FWHM values of $Cs_2NaCeI_6$, fit using eq S1.

(Eq. S1) $$\mathrm{FWHM}(T)=2.36\sqrt{S}\hbar\omega\sqrt{\coth\left(\frac{\hbar\omega}{2k_bT}\right)}$$

(Eq. S2) $$\Delta E_S = (2S-1)\hbar\omega$$

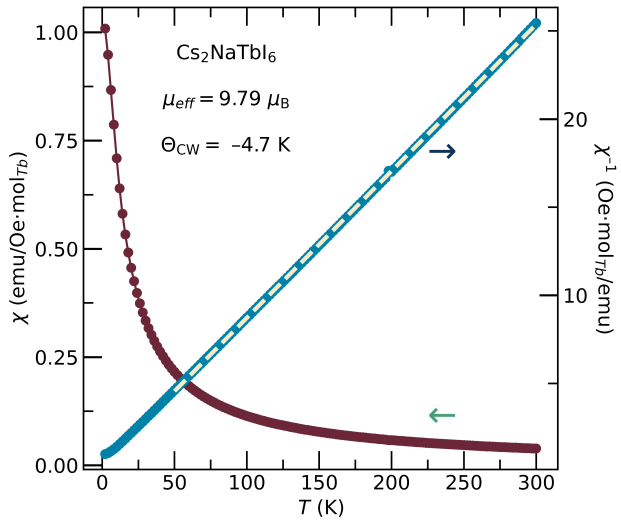


**Figure S9.** Magnetic susceptability (χ, left y-axis) vs temperature plot and inverse magnetic susceptability ($\chi^{-1}$, right y-axis) vs temperature plot with CW fit (dashed line) of $Cs_2NaTbI_6$.

**Table S5.** Summary of Curie-Weiss Law fit parameters.

| Compound | $Cs_2NaCeI_6$ | $Cs_2NaNdI_6$ | $Cs_2NaGdI_6$ | $Cs_2NaTbI_6$ | $Cs_2NaDyI_6$ |
|---|---|---|---|---|---|
| $\mu_{eff}$ ($\mu_B$ per *Ln*) | 2.67 | 3.76 | 8.24 | 9.79 | 10.98 |
| $\theta_{cw}$ (*K*) | N.D. | N.D. | 0.3 | –4.7 | –5.0 |
| $\chi^0$ (emu/Oe·mol) | –0.0002 | –0.00025 | –0.0004 | –0.0004 | –0.0004 |

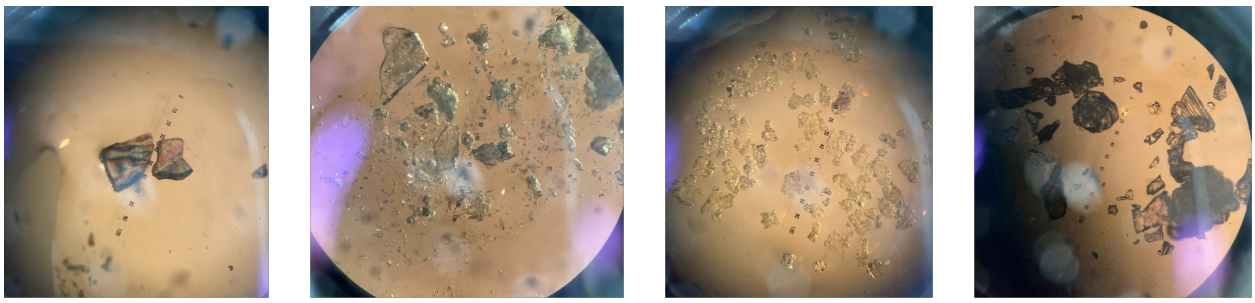

**Figure S10.** Images of $Cs_2NaLnI_6$ crystals (Ln = Ce, Nd, Tb, Dy; in order from left to right, respectively), the distance between each tick mark is 13.3 microns.

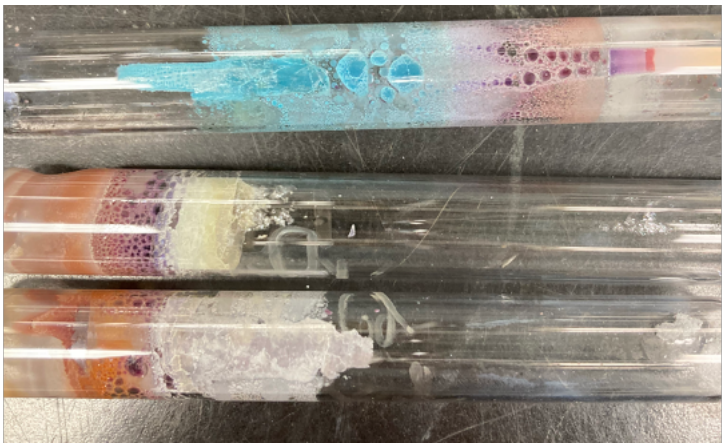

**Figure S11.** Image of example self-flux/transport of $Cs_2NaLnI_6$ (Ln = Nd, Dy, Gd; in order from top to bottom, respectively).

**References**:


(1) Perl, J.; Shin, J.; Schümann, J.; Faddegon, B.; Paganetti, H. TOPAS: An Innovative Proton Monte Carlo Platform for Research and Clinical Applications. *Med. Phys.* **2012**, *39* (11), 6818–6837.
(2) SMART Apex II, Version 2.1 Ed.; Bruker AXS Inc.: Madison WI, 2005.
(3) SAINT Software User's Guide, Version 7.34a Ed.; Bruker AXS Inc.: Madison, WI, 2005.
(4) Sheldrick, G. M. SADABS, the Siemens Area Detector Absorption Correction; University of Göttingen: Göttingen, Germany, 2005.
(5) SHELXTL PC, Version 6.12 Ed.; Bruker AXS Inc.:Madison, WI, 2005.